International Journal of Greenhouse Gas Control 53 (2016) 230–242

Contents lists available at ScienceDirect

International Journal of Greenhouse Gas Control

journal homepage: www.elsevier.com/locate/ijggc

Convective dissolution of CO_2 in reactive alkaline solutions: Active role of spectator ions

C. Thomas*, V. Loodts, L. Rongy, A. De Wit

Université libre de Bruxelles (ULB), Faculté des Sciences, Nonlinear Physical Chemistry Unit, CP231, 1050 Brussels, Belgium

ARTICLE INFO

Article history:
Received 19 December 2015
Received in revised form 23 May 2016
Accepted 21 July 2016

Keywords:
Convective dissolution
Fingering
Reactive dissolution
CO_2 sequestration

ABSTRACT

Upon dissolution of carbon dioxide (CO_2) into deep saline aquifers, various chemical reactions are likely to take place between dissolved CO_2 and reactants dissolved in the brine, which may drastically impact the mixing of stored CO_2 in the reservoir. Our objective is to understand how the nature of the dissolved chemical reactants affects the convective dynamics generated by the dissolution of CO_2 into the host phase. To do so, we study experimentally in a Hele-Shaw cell the reactive and convective dissolution of gaseous CO_2 into aqueous solutions of bases MOH where M^+ is an alkali metal cation. We quantify the effect of the counter-ion M^+ on the convective dynamics. Using a schlieren optical setup, we compare the convective patterns in pure water to those in different alkaline solutions of various concentrations. For any reactant MOH studied, the fingering instability develops faster in the reactive case than in pure water, and convection is enhanced if the concentration of the reactant is increased. Furthermore, changing the counter-ion M^+ modifies the onset time and the non-linear development of the fingering instability. We explain these experimental results by theoretically analyzing the reaction–diffusion density profiles developing in the solution. We find that changing the counter-ion M^+ of the base modifies the density profile, not only through solutal effects but also through differential diffusivity effects. This highlights that the spectator ion M^+, despite not participating actively in the acid–base reaction, impacts the development of the hydrodynamic instability. Our results suggest that, in the context of CO_2 sequestration, the details of the chemical composition of the storage site should be taken into account for more accurate modeling of the reactive transport of dissolved CO_2.

1. Introduction

The dissolution of CO_2 into deep saline aquifers can lead to a buoyantly unstable stratification of denser CO_2-enriched brine on top of less dense pure brine, giving rise to density-driven convective mixing in the host phase (Ennis-King and Paterson, 2005; Emami-Meybodi et al., 2015). Transport by convection, which is orders of magnitude faster than transport by molecular diffusion, is a process favorable to the sequestration of CO_2 as it can significantly enhance the dissolution rate of CO_2 into the brine (Ennis-King and Paterson, 2005; Hassanzadeh et al., 2005; Neufeld et al., 2010; Mojtaba et al., 2014), reducing mixing times from thousands to hundreds of years (Backhaus et al., 2011).

Upon dissolution of CO_2 in the aquifer, a variety of geochemical reactions may occur between dissolved acidic CO_2 and reactants dissolved in the brine (Rochelle et al., 2004; Emami-Meybodi et al., 2015). These reactions can modify the density profile in the host aqueous phase, and thereby the unstable density stratification that triggers convective motions in the brine. The impact of these reactive processes on the transport of CO_2 in the reservoir is, however, poorly understood. Most numerical studies working on dissolution-driven convection in storage sites indeed simply disregard the influence of chemical reactants and products on the fluid density (Zhang et al., 2011; Xu et al., 2012; Tian et al., 2014).

Some studies have focused on the stabilizing effect of a chemical reaction on convective dissolution, showing that a reaction between CO_2 and the solid porous matrix reduces the unstable density gradient. This restrains the penetration of CO_2 fingers into the underlying brine and delays the onset of convection (Andres and Cardoso, 2011, 2012; Ghesmat et al., 2011; Cardoso and Andres, 2014; Kim and Choi, 2014; Ward et al., 2014a,b; Kim and Kim, 2015). However, density changes due to the consumption of CO_2 may not be the only effect of the reaction, as variations in the concentrations of other dissolved reactants and products can also affect density, and thus convection (Ennis-King and Paterson, 2007; Wylock et al., 2014).

* Corresponding author.
E-mail addresses: cathomas@ulb.ac.be (C. Thomas), adewit@ulb.ac.be (A. De Wit).

http://dx.doi.org/10.1016/j.ijggc.2016.07.034
1750-5836/

In parallel, Budroni et al. (2014) considered a partially miscible liquid/liquid system which can be seen as an analogue for studying the dissolution of CO_2 in water. Specifically, they analyzed the stratification of an ester above water, in which the ester dissolves and undergoes a hydrolysis reaction. Density-driven fingering occurs, driven by the solubilization process of the ester into the water layer. In this partially miscible system, they showed that an $A+B \rightarrow C$ chemical reaction can have a stabilizing effect on convection even when both B and C contribute to the density profile. Indeed, the replacement of reactant B by a less dense salt C in the host phase creates a minimum of density below the interfacial region, which refrains the development of fingers.

In fact, depending on the physico-chemical characteristics of the reservoir, chemical reactions could be beneficial for or unfavorable to the dissolution of CO_2. We have shown recently by means of a linear stability analysis that a general $A+B \rightarrow C$ chemical reaction can either increase or decrease the intensity of convective dissolution in partially miscible systems, depending on how the reaction product influences the local density with respect to the initially dissolved reactant (Loodts et al., 2014a, 2015). We have also demonstrated experimentally that, in a gaseous CO_2–water system, enhanced convection can be obtained by dissolving CO_2 into aqueous solutions of NaOH (Loodts et al., 2014a). Furthermore, increasing the concentration of the reactant in the host aqueous solution favors the development of convective fingering. However, we only focused on NaOH solutions without varying the nature of the base and did not take differential diffusivity into account in the theoretical interpretation of the results. Furthermore, due to the weak sensitivity of our visualization system we were not able to compare the fingering dynamics in aqueous NaOH to that developing in water.

It has been shown in fully miscible systems that the nature of the species involved in the reaction can influence convective mixing rates. Indeed, Almarcha et al. (2011) have demonstrated both experimentally and theoretically that the convective regimes triggered by $A+B \rightarrow C$ reactions in miscible systems depend on the type and concentration of the reactants. In particular, they observed that diverse patterns can be obtained during the neutralization of a strong acid HCl by various strong bases MOH in aqueous solutions, depending on the solutal expansion and diffusion coefficients of the chemical species in the solution. In other words, they showed that changing the counter-ion M^+ of the basic reactant MOH drastically impacts convection upon contact between the two miscible solutions.

In this context, our objective is to understand how convective dissolution in the partially miscible CO_2–water system is influenced by the nature of the reactants involved. In a Hele-Shaw cell, the density-driven instability induced by the dissolution of CO_2 in water is compared with that induced in various aqueous alkaline solutions. With a high-sensitive schlieren imaging system, the convective dynamics is followed over time in water and in solutions containing increasing concentrations of LiOH, NaOH, KOH and CsOH. In order to determine whether and how the chemical nature and concentration of the base in solution influence the observed pattern, the evolution of the fingered zone is analyzed quantitatively over time. We find that the development of the instability strongly depends on the concentration of the base in solution, and, to a lesser extent, on the nature of the counter-ion M^+, even if this spectator ion does not participate in the chemical reaction. If the concentration of reactant MOH is increased, the onset time of convection is shorter and the instability develops faster. Similarly, convection is intensified if the counter-ion of the hydroxide is an element of the alkaline column with a larger atomic mass ($Li^+ < Na^+ < K^+ < Cs^+$). On the basis of a reaction–diffusion model including the effect of an $A+2B \rightarrow C$ reaction, we enlighten the experimental results by the analysis of the numerical density profiles developing in the aqueous phase. The solutal Rayleigh numbers and the diffusivity ratios have been computed with the parameters used in experiments. In particular, we show that differential diffusion is crucial to understand the experimental findings.

The paper is organized as follows: first, in Section 2, we present the experimental setup and methods. Then the development of the convective instability generated by the dissolution of CO_2 in water and in various alkaline solutions of increasing concentration is analyzed qualitatively and quantitatively in Sections 3 and 4, respectively. In Section 5, the density profiles corresponding to the various concentrations and bases used in experiments are computed. A discussion of the relative effects of solutal and diffusion coefficients is found in Section 6. The experimental results are interpreted in light of the theoretical analysis in Section 7. Finally, the conclusions from this study are summarized in Section 8.

2. Experimental setup

Experiments are carried out at room temperature in a Hele-Shaw cell composed of two 210 mm × 260 mm × 6 mm flat glass plates maintained parallel and vertical in the gravity field (Fig. 1). The plates are separated by a rigid spacer giving a gas-tight inner space between the glass plates of 165 mm × 210 mm × 0.5 mm. The cell is partially filled with aqueous solutions through the inlet at the bottom of the cell. Two upper inlets are used to let gases (N_2 or CO_2) flow in and out of the cell at a constant flow rate (6.0 L/h). The gaseous phase inside the cell is kept at atmospheric pressure as the excess of gas is continually evacuated.

Solutions of LiOH, NaOH, KOH (solid form, purity ≥ 98%, Sigma–Aldrich) and CsOH (liquid form, 50% wt in H_2O, purity ≥99.9%, Sigma–Aldrich) are prepared with deionized water.

For the reproducibility of initial conditions, all experiments were conducted following the same protocol. First, the cell is purged with gaseous N_2 to avoid the presence of atmospheric CO_2 in the cell. The cell is then partially filled from the bottom with 15 ml of either pure water or an aqueous solution of the alkali MOH. N_2 is then replaced by CO_2 in order to start the experiment. The time $t = 0$ s is fixed as the time of the switch of N_2 to CO_2 in the system. Note that as all gases flow at the same rate, no disturbance of the interface is observed at the beginning of the experiment.

To avoid any effect of a color indicator on the dynamics (Almarcha et al., 2010; Kuster et al., 2011; Thomas et al., 2015), a schlieren visualization technique (Settles, 2001) is used to track the convective patterns in the transparent aqueous solutions. This optical technique, schematically depicted in Fig. 1, provides a

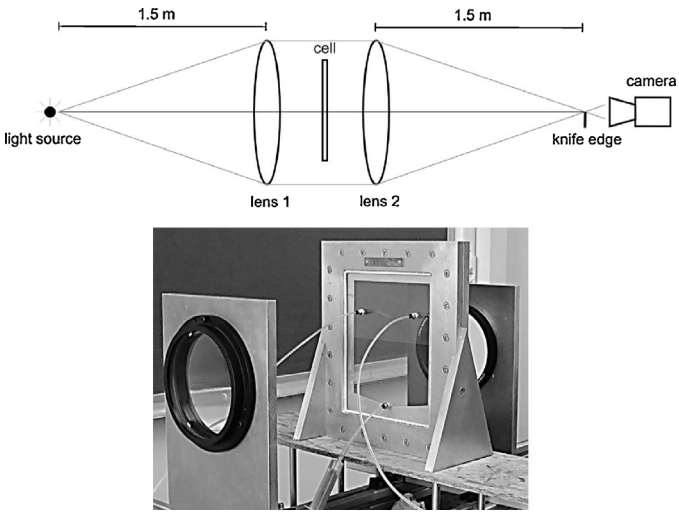

Fig. 1. Top: schematic of the schlieren setup. Bottom: photo of the Hele-Shaw cell, placed between the two optical lenses.

visualization of gradients of refractive index related to density gradients, and allows to follow the dynamics in real time without interfering with it. Our schlieren system consists of an alignment of: a light source; two achromatic lenses of diameter 15 cm with 1.5 m focal length, between which the Hele-Shaw cell is placed; a knife edge; and a video camera to record the dynamics every 2 s during the experiment.

To analyze the experimental data, the recorded images are cropped to select the area where the dynamics takes place. Pictures are converted to gray-level images and divided by a reference image, taken before the introduction of CO_2 in the cell.

3. General development of the fingering instability

Figs. 2a and b show the temporal development of the density-driven fingering generated by the dissolution of gaseous CO_2 into deionized water, i.e., the non-reactive case. Before the injection of CO_2 in the head-space of the cell, the schlieren images of the aqueous solution are uniformly gray and the interface between the gas and the aqueous phases is flat. A few minutes after the beginning of the experiment, a thin CO_2-enriched boundary layer develops below the interface and grows diffusively over time. This thin layer is later destabilized into fingers sinking from the interface (see Fig. 2a). Over time, fingers grow, enlarge and sometimes merge (Fig. 2b). They also lose their contrast due to the decrease of density gradients (and thus of refractive index gradients) resulting from the mixing of the dissolved species in water.

The convective dynamics in water is compared at 13 min to the one in a reactive solution of LiOH 0.01 M (Fig. 2b and c). In the reactive case, fingers are larger, more extended and even feature some tip splitting. Convection appears sooner in the reactive solution and develops faster than in water. In LiOH solutions, the denser CO_2-enriched boundary layer developing below the interface appears immediately after the injection of gaseous CO_2 in the cell and is more contrasted than in water. This denser layer becomes thicker in time and is readily destabilized into many fingers sinking from the interface. Non-linear effects like merging appear rapidly after the onset of convection followed later in time by tip splitting in reactive experiments only (Fig. 2c). Those phenomena will be further discussed in Section 4.2.

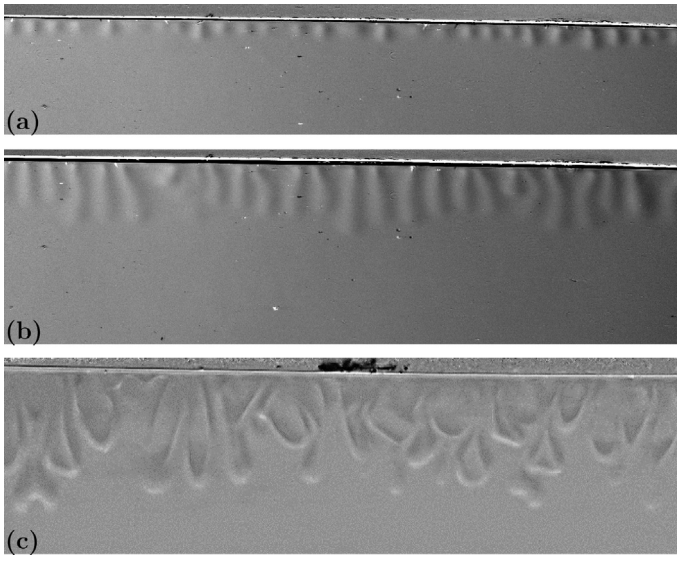

Fig. 2. Comparison of the density-driven convection generated by the dissolution of CO_2 in water at (a) $t = 6$ min, (b) $t = 13$ min; and (c) in a solution of LiOH 0.01 M at $t = 13$ min. Dimensions are 8.6 cm × 1.7 cm for (a) and 8.6 cm × 2.5 cm for (b) and (c).

The general development of the instability depends on the type of reactant MOH involved and on its initial concentration. In order to evaluate both effects, we first vary the concentration of each base in solution. We then compare the convective pattern generated by the dissolution of CO_2 in various solutions of strong bases at fixed concentration (see examples of the dissolution of CO_2 in solutions of LiOH, NaOH, KOH and CsOH 0.05 M, in the videos provided in the Supplementary Material).

3.1. Effect of the concentration

In order to study the influence of the concentration of the base on the dynamics, four concentrations are considered for each base: 0.01 M, 0.02 M, 0.05 M and 0.1 M. Fig. 3 shows a selection of fingering patterns observed at $t = 13$ min in solutions of LiOH, NaOH, KOH and CsOH for two different concentrations (0.01 M and 0.1 M). It can be seen that fingers appear sooner and sink faster when the concentration of the base is increased. Merging, splitting and other finger interactions appear also more frequently in more concentrated solutions. In good agreement with the theory developed by Loodts et al. (2014a, 2015), the convective instability is strongly intensified when the concentration of the reactant is increased in the aqueous phase.

We also observe a black layer developing below the interface in concentrated CsOH solutions, with a thickness of a few mm growing diffusively over time. The extent of this dark layer seems to increase with the concentration of the base and is not observed in 0.01 M and 0.02 M solutions. Several tests have been performed to understand the origin of this dark layer. The experiment with the highest concentration of CsOH was conducted with an infrared camera but no change in temperature larger than 0.1 K was noticed in the solution. Moreover, the development of a dark layer was also observed in experiments with other bases at higher concentrations. We therefore conclude that the black layer developing in experiments at high concentrations corresponds most probably to the accumulation of the product of the reaction below the interface which has a refractive index different from the reactants.

3.2. Effect of the counter-ion M^+

We now focus on the influence of the chemical nature of the base on the convective dissolution of CO_2 in aqueous reactive solutions. More specifically, we change the counter-ion M^+ of the hydroxide anion OH^- in the reactive solution, and qualitatively compare in Figs. 3 and 4 the temporal evolutions of fingers in solutions of LiOH, NaOH, KOH and CsOH at a fixed concentration. Even if the dynamics are similar in all aqueous solutions, the fingering instability appears sooner and develops faster as we go down in the column of alkali metals. In other words, convection is enhanced in the series $Li^+ < Na^+ < K^+ < Cs^+$. We comment further below on how this trend is influenced by the concentration of the base.

4. Quantitative analysis of the fingering dynamics

An image processing of the experimental results has been performed with Mathematica to analyze quantitatively the development of the fingering dynamics over time. First, the area of interest is defined for each experiment by selecting on the last picture recorded the largest rectangle starting from the interface in which the dynamics takes place. Considering the sensitivity of schlieren systems to vibrations generating a large variable noise, further image enhancement involving Gaussian filters had to be performed to reduce the noise and smooth the gray-level pictures as much as possible.

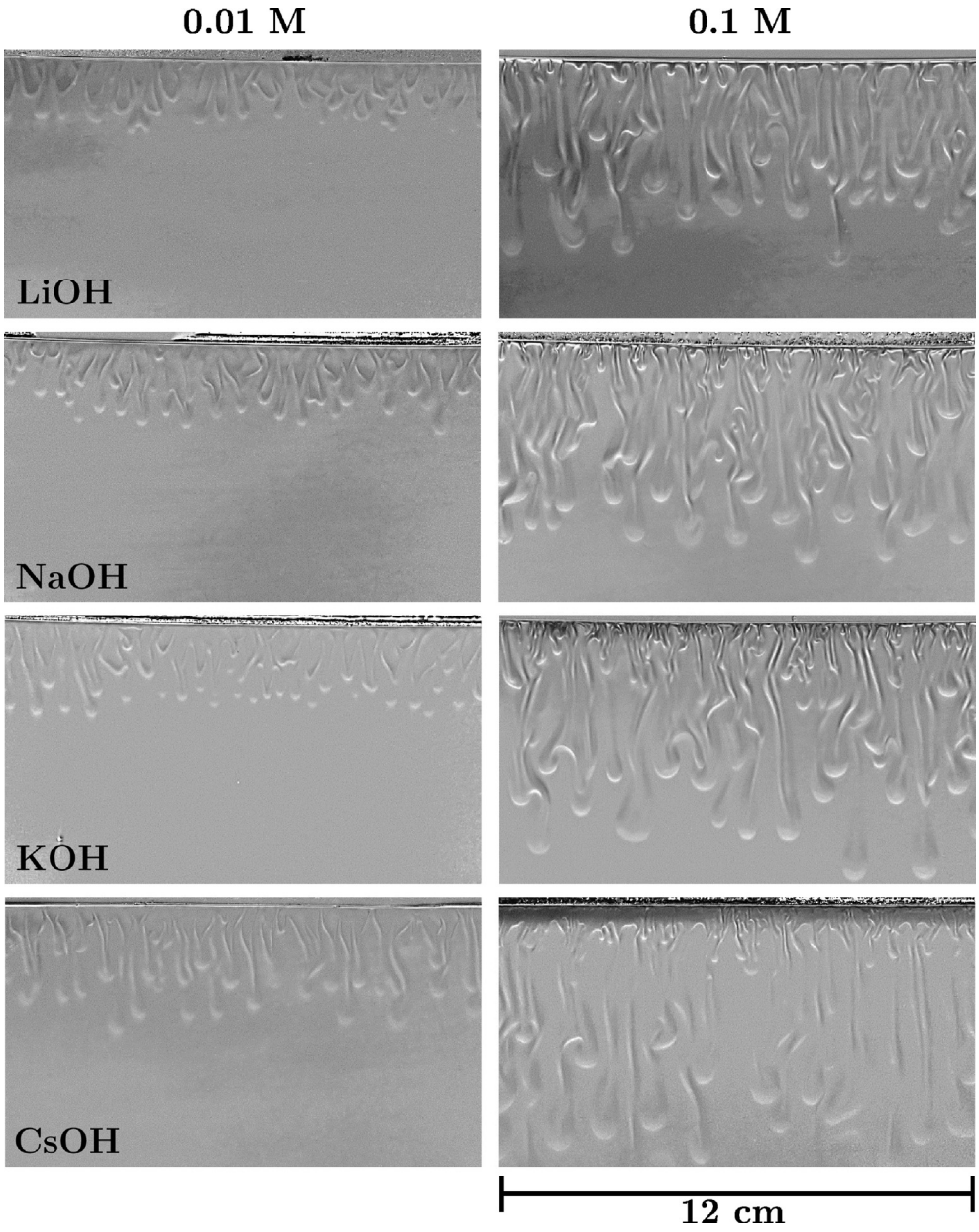

Fig. 3. Fingering patterns recorded at $t = 13$ min in solutions of LiOH, NaOH, KOH and CsOH at 0.01 M and 0.1 M. The field of view is 12 cm × 7 cm.

4.1. Mixing length

The resulting processed pictures are then converted to black and white binary pictures to compute the evolution of the mixing length L, defined as the length of the convective zone (see Fig. 5), and computed as the length of the longest finger growing from the interface. The convective pattern appears white on the binarized pictures but, over time, only the more contrasted parts of the fingers remain visible. Indeed, due to diffusion, fingers become less contrasted over time, and the binarization and noise reduction processes lead inevitably to the loss of some information. However, the tip of fingers remains clearly defined over time and its position is used to compute the mixing length.

To begin with, the position of the interface between the gas and the liquid is defined on the first picture of each experiment as the brightest horizontal line on the image. Then, the position of the tip of the longest finger is computed on every picture by finding the position of the vertical white element which is the farthest away from the interface (see example in Fig. 5). For each time, the mixing length L is computed as the difference between this position and that of the interface. This process was not possible for the non-reactive case, where the density gradients are too small to be automatically detected. Therefore, the evolution of L has been computed in this non-reactive case by measuring manually the distance between the interface and the tip of the longest finger as a function of time. Finally, temporal evolutions of the lengths obtained for five experiments are averaged.

An example of the results obtained for five experiments with LiOH 0.05 M and the corresponding averaged mixing length is shown in Fig. 6. The averaged mixing lengths obtained for water and for different bases in increasing concentrations are compared over time in Fig. 7.

The temporal evolution of L observed in Fig. 7 is typical of the convection developing in partially miscible systems. Upon dissolution of gaseous CO_2 in the aqueous solution, a thin denser layer develops below the interface, the length of which grows as a square

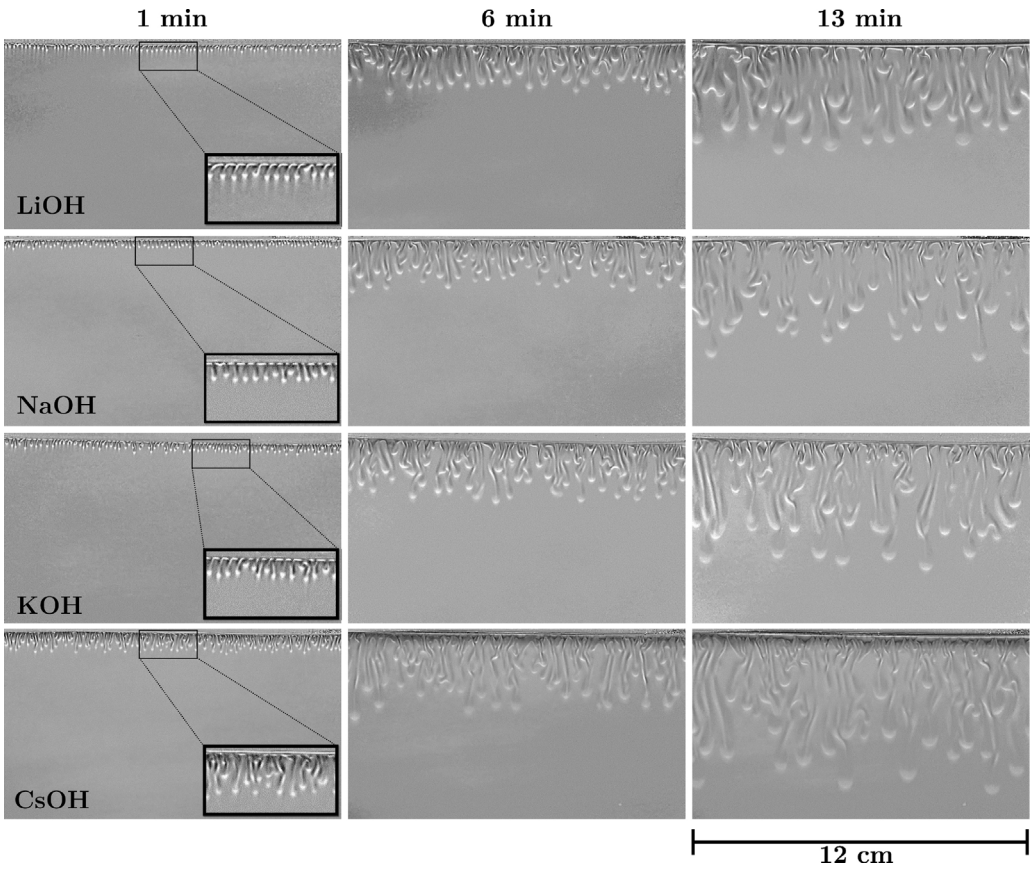

Fig. 4. Development of density-driven instabilities over time induced by the dissolution of gaseous CO_2 in aqueous solutions of LiOH, NaOH, KOH and CsOH in concentration 0.05 M. The field of view is 12 cm × 7 cm, the zoom on the fingers at t = 1 min is 2 cm × 1 cm.

root of time in the diffusive regime, as long as the system remains stable. When convection sets in, the formation of fingers sinking from the interface accelerates the penetration of dissolved CO_2 in the solution, and L increases then faster until the end of the experiment (Fig. 7). Sometimes, a finger develops faster than the other ones but this single finger generally slows down after some time or even stops growing, before it gets dragged into the flow generated by the other growing fingers. In that case, the evolution of L can be seen to slow down for some time before it accelerates again. This effect is damped by averaging the mixing lengths on several experiments but can be noticed in some regions of Fig. 7, for instance on the mixing length of CsOH, Fig. 7d between t = 400 s and t = 500 s.

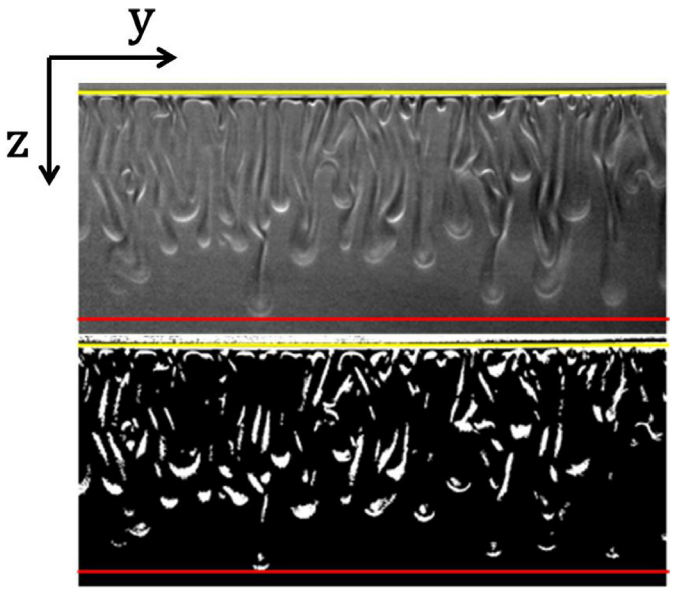

Fig. 5. Gray-level picture (top) and corresponding binarized picture (bottom) of convective fingers in a solution of LiOH 0.1 M at t = 13 min. The distance between the interface (upper yellow line) and the line passing along the longest finger (bottom red line) defines the mixing length. (For interpretation of the references to color in this figure legend, the reader is referred to the web version of the article.)

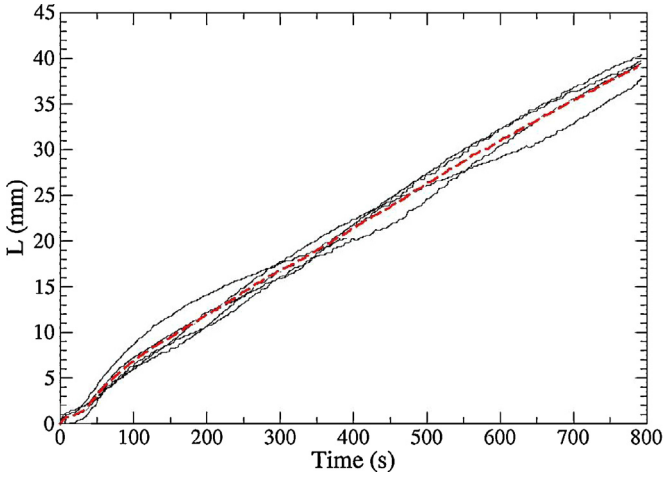

Fig. 6. Temporal evolution of the mixing lengths for five experiments of CO_2 dissolution in LiOH 0.05 M solutions. The red dashed curve represents the average of the five experiments. (For interpretation of the references to color in this figure legend, the reader is referred to the web version of the article.)

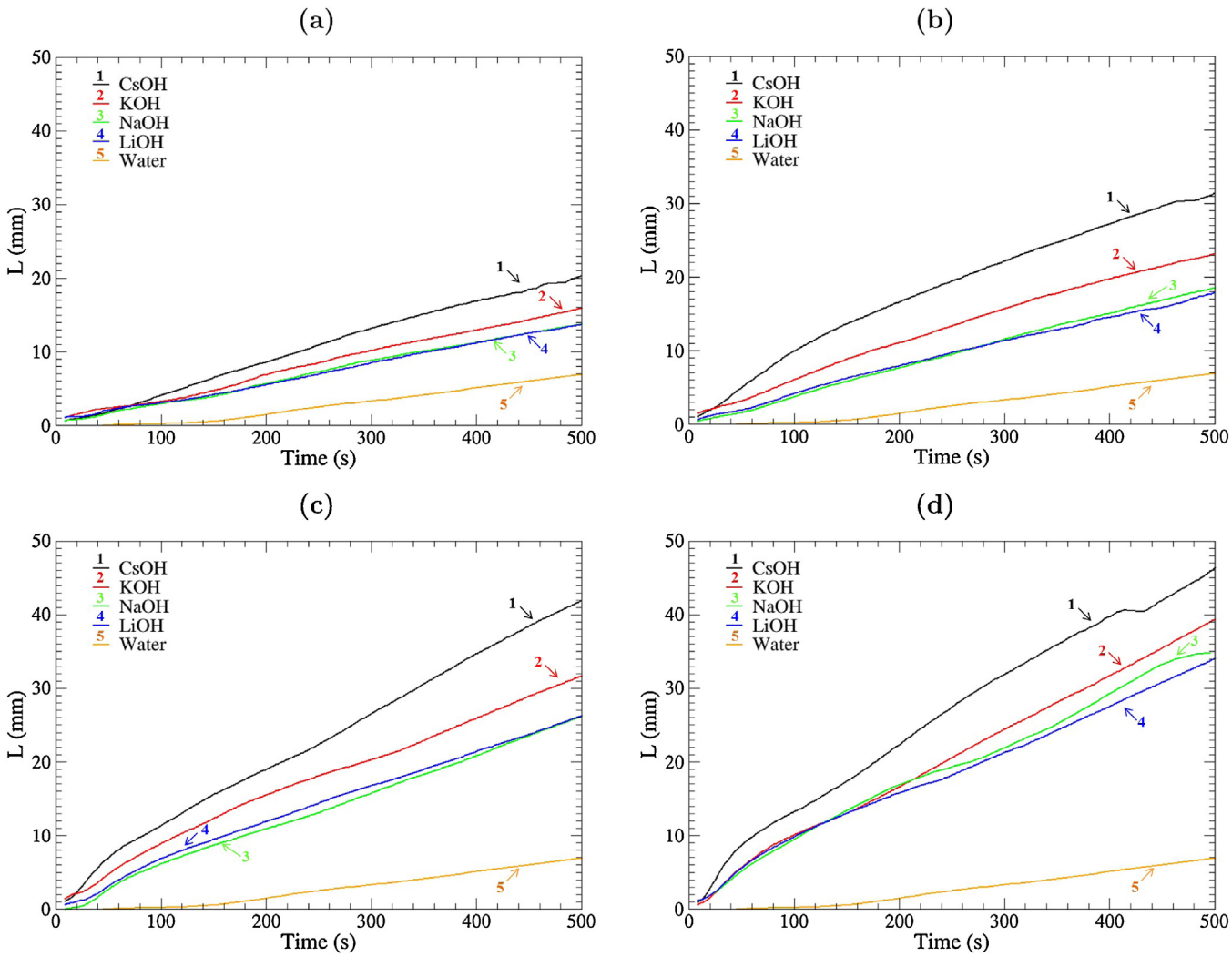

Fig. 7. Temporal evolution of the mixing length in water or in aqueous solutions for various base concentrations: (a) 0.01 M; (b) 0.02 M; (c) 0.05 M; (d) 0.1 M. Each curve represents the average of five experiments.

The characteristic onset time of convection (i.e. the time at which the evolution of L departs from the diffusive trend) is shorter when the concentration of the base is increased. Moreover, at a fixed concentration, the onset time is similar for LiOH, KOH and NaOH solutions, but is always shorter for CsOH solutions in which fingers are observed to appear sooner. As expected from Figs. 3 and 4, fingers also grow faster in CsOH solutions. For every concentration, the mixing length of fingers in CsOH solutions is always larger than in other solutions at a given time. The slowest evolutions are observed in LiOH solutions, where the fingers can reach final lengths up to 15 mm smaller than in CsOH solutions at $t = 500$ s (see for example Fig. 7c). However, the evolution of L is very similar for LiOH and NaOH solutions for every concentration tested.

To compare the speed of the convective fingers after the onset of convection, their averaged velocities are obtained in water and in different reactive solutions. To do so, the averaged slope of the temporal evolution of L is computed between $t = 100$ s and $t = 500$ s for water and for the different bases in increasing concentration (Fig. 8). The averaged velocity of fingers sinking in water is the lowest. The largest velocities are observed in the most concentrated reactive solutions. For every concentration of base, fingers sink at similar speeds in LiOH and NaOH solutions, and a little faster in KOH solutions where, at 0.1 M, velocities are up to 0.5 mm/min larger than in LiOH and NaOH solutions. Finally, fingers are always between 1 and 2 mm/min faster in CsOH solutions than in LiOH solutions.

These results confirm the observations made in Figs. 3 and 4. Convection is clearly enhanced when the concentration of the base is increased. Furthermore, at a fixed concentration, the convective instability starts sooner and the vertical velocity of fingers is larger in CsOH solutions than in other bases. In general, convection is enhanced in the sequence LiOH < NaOH < KOH < CsOH.

4.2. Space–time maps

To study the dynamics and the movement of fingers just below the interface, we draw space–time maps of the location of fingers by plotting as a function of time the pixel intensities along the horizontal line 2 mm below the interface on the gray-level pictures. A selection of space–time maps obtained for KOH solutions in increasing concentration is presented in Fig. 9. First, we see that interactions between fingers near the interface are almost absent in 0.01 M solutions, for the 800 s period of time considered here (Fig. 9a). Fingers may interact further down in the solution, but their base line remains at the same location until the end of the experiment, independently of their neighbors.

When the concentration of the base is increased, more complicated structures start to appear in the space–time maps. In more reactive solutions, the system enters in a non-linear regime rapidly

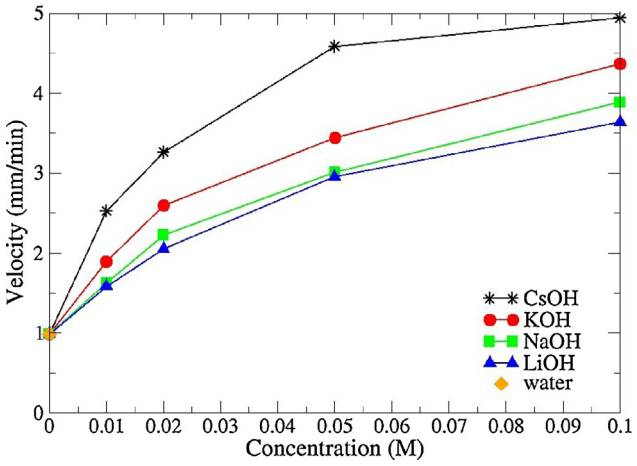

Fig. 8. Averaged vertical velocities computed from the averaged slope of the evolution of the mixing length L between $t = 100$ s and $t = 500$ s for water and for LiOH, NaOH, KOH and CsOH in increasing concentration. The points were connected just to guide the eye.

after the onset of convection. The system is more unstable and hence the number of fingers merging and splitting is increased with regard to the CO_2–water system. In 0.05 M and 0.1 M solutions, a repetitive production of fingers is observed over time, which sustains the convective dynamics in the bulk. Indeed, as shown in Fig. 9c and d, a series of new fingers appearing regularly can be noticed at some locations. The time interval between successive finger births becomes smaller when the concentration of KOH increases. As the time step between two horizontal lines is 2 s, this period of fingers birth can be measured and is about 60 s for KOH 0.05 M (Fig. 9c), and 30–35 s for KOH 0.1 M (Fig. 9d). For lower concentrations, this production of new fingers is less frequent and is barely visible on the space–time maps. Note also that the wavelength of the pattern at early times is larger for small concentrations. Indeed, from 0.01 M to 0.1 M, the wavelength decreases from 3.4 mm (Fig. 9a) to 1.2 mm (Fig. 9d).

From our observations, similar descriptions can be made for space–time maps of other bases. Some details can differ in the evolution of the dynamics if the base is changed, specifically for 0.1 M, as shown in Fig. 10 which represents space–time maps of the location of fingers below the interface in solutions of CsOH, KOH, NaOH and LiOH at 0.1 M. In the case of CsOH, the map appears very dark because of the dark layer developing below the interface (see Fig. 3), which makes the analysis impossible after some time in that location. Nevertheless, the dynamics near the interface is intrinsically different if the nature of the base is changed. The time interval at which new fingers appear slightly increases from ~30–35 s for KOH to ~40–45 s for NaOH and LiOH. The wavelength of the pattern at early times does not vary significantly from one base to another. At onset, the measured wavelength is of 1.3 mm for CsOH and KOH solutions and 1.6 mm for LiOH and NaOH. Fewer fingers are indeed observed at the onset of convection in NaOH and LiOH than in KOH and CsOH solutions. Over time, the wavelength increases in all cases. For example, in the case of LiOH, the wavelength at the onset of convection is 1.6 mm whereas it is 4.8 mm at the end of the experiment. This change in the wavelength can be related to the general coarsening trend that is observed in all cases once the instability develops. Following the onset of convection, fingers appear, start to grow and move laterally to merge with the closest neighbor. When the distance between two fingers is large, a new finger appears in the boundary layer between existing fingers and follows the same behavior. Some preferred pathways can be observed, as new fingers emerging from a given area are always attracted to the same finger.

5. Density profiles

The development of density-driven fingering depends on the density stratification in the host aqueous solution, built before the onset of convection, i.e. when the velocity field in the aqueous solution is equal to zero. Therefore, to understand the experimental results, we follow the reasoning of Almarcha et al. (2011) and compute the numerical one-dimensional (1D) reaction–diffusion (RD) density profiles in the aqueous solution corresponding to the various concentrations and bases used in the experiments.

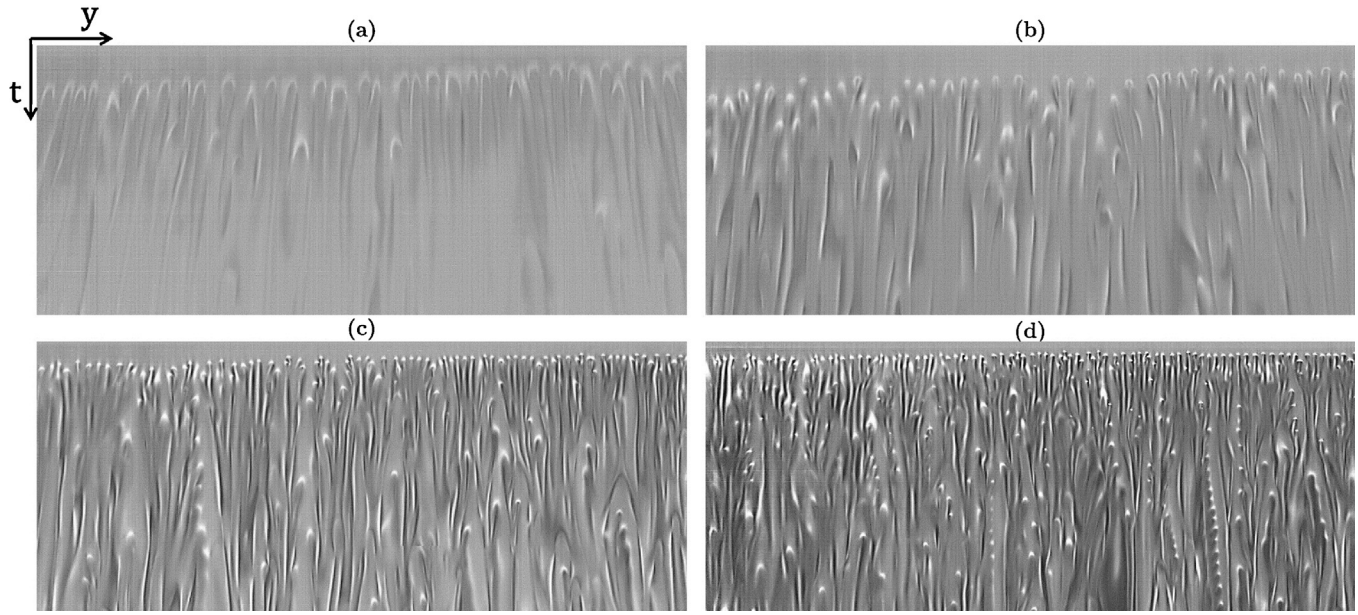

Fig. 9. Space–time maps of the location of fingers at a fixed depth (2 mm below the gas–liquid interface) as a function of time in solutions of KOH in increasing concentration (a) 0.01 M; (b) 0.02 M; (c) 0.05 M; (d) 0.1 M. Time is running downwards, the width is 12 cm and $t_{max} = 800$ s.

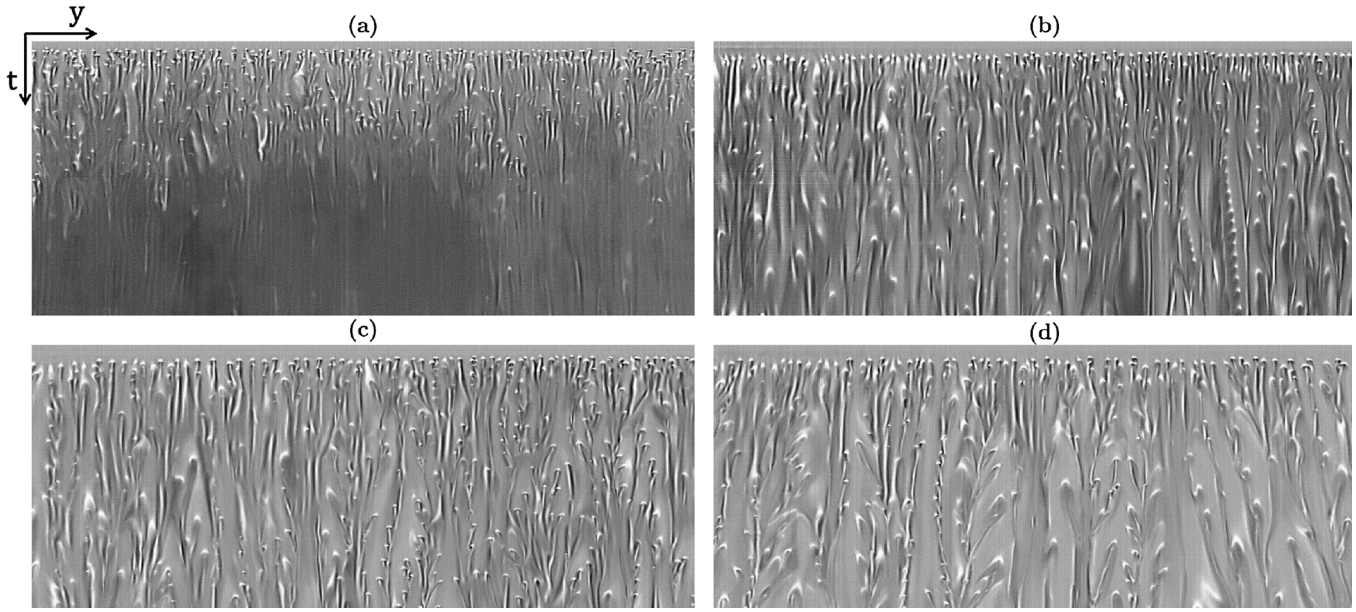

Fig. 10. Space–time maps of the location of fingers at a fixed depth (2 mm below the gas–liquid interface) as a function of time in solutions of (a) CsOH; (b) KOH; (c) NaOH; (d) LiOH at a fixed concentration of 0.1 M. Time is running downwards, the width is 12 cm and t_{max} = 800 s.

5.1. Theoretical model

The density profile in the aqueous solution depends on the concentration profiles of the different chemicals. In this section, we describe the theoretical model used to compute such concentration profiles numerically.

5.1.1. Reaction scheme

When gaseous CO_2 fills the head-space of the cell, it dissolves with a finite solubility A_0 into the underlying aqueous solution where it slowly diffuses downwards. Dissolved CO_2 reacts with water to form carbonic acid (H_2CO_3), which instantaneously dissociates into bicarbonate (HCO_3^-) and carbonate (CO_3^{2-}) ions, following the equilibrium equations:

$$CO_{2(g)} \rightleftharpoons CO_{2(aq)} \quad (1)$$

$$CO_{2(aq)} + H_2O_{(l)} \rightleftharpoons H_2CO_{3(aq)} \quad (2)$$

$$H_2CO_{3(aq)} \rightleftharpoons H^+_{(aq)} + HCO^-_{3(aq)} \quad (3)$$

$$HCO^-_{3(aq)} \rightleftharpoons H^+_{(aq)} + CO^{2-}_{3(aq)} \quad (4)$$

Equilibrium (2) is often not mentioned in studies of the absorption of gaseous CO_2 in aqueous solutions (Hikita et al., 1976; Pohorecki and Moniuk, 1988; Vas Bhat et al., 2000; Wylock et al., 2011). Carbonic acid is indeed unstable in water and is present only in small amounts in aqueous solutions (Loerting et al., 2000). Following usual conventions (Zeebe and Wolf-Gladrow, 2001), the notation $CO^*_{2(aq)}$ is used to represent both dissolved $CO_{2(aq)}$ and carbonic acid in water, and we can thus combine reactions (2) and (3) into:

$$CO^*_{2(aq)} + H_2O_{(l)} \rightleftharpoons H^+_{(aq)} + HCO^-_{3(aq)} \quad (5)$$

Furthermore, it can be shown that in pure water at room temperature and for a CO_2 pressure of 1 atm, $CO^*_{2(aq)}$ does not decompose significantly into $HCO^-_{3(aq)}$ and $CO^{2-}_{3(aq)}$ (Zeebe and Wolf-Gladrow, 2001). We can thus assume that, for the non-reactive case, the only species dissolved in water is $CO^*_{2(aq)}$, as typically done in interpretations of experimental studies on CO_2 convective dissolution (Kneafsey and Pruess, 2010, 2011; Faisal et al., 2013, 2015; Outeda et al., 2014).

Table 1
Initial concentrations B_0 of reactant B = MOH, used in the experiments, and corresponding dimensionless ratios $\beta = B_0/A_0$ where A_0 = 0.038 M is the solubility of CO_2 in water for a pressure of gaseous CO_2 of 1 atm and a temperature of 20 °C.

B_0 (M)	β
0.01	0.26
0.02	0.52
0.05	1.31
0.1	2.61

In the reactive case, a base MOH, with M^+ an alkali metal cation Li^+, Na^+, K^+, or Cs^+, is initially dissolved in the host aqueous solution with an initial concentration B_0 (see Table 1). The following acid–base reactions take thus place in the host aqueous solution:

$$CO^*_{2(aq)} + MOH_{(aq)} \underset{k_{12}}{\overset{k_{11}}{\rightleftharpoons}} MHCO_{3(aq)} \quad (6)$$

$$MHCO_{3(aq)} + MOH_{(aq)} \underset{k_{22}}{\overset{k_{21}}{\rightleftharpoons}} M_2CO_{3(aq)} + H_2O_{(l)} \quad (7)$$

The values of the kinetic constants (Wylock et al., 2011; Gondal et al., 2015) shown in Table 2 suggest that reactions (6) and (7) can be considered as irreversible ($k_{11} \gg k_{12}$ and $k_{21} \gg k_{22}$) and that reaction (6) is the limiting step of the reaction scheme ($k_{11} \ll k_{21}$) (Pohorecki and Moniuk, 1988). Therefore, the total reaction scheme can be simplified to (Hikita et al., 1976):

$$CO^*_{2(aq)} + 2MOH_{(aq)} \overset{k_{11}}{\rightarrow} M_2CO_{3(aq)} + H_2O_{(l)}, \quad (8)$$

with a reaction rate equal to the rate of reaction (6), $k_{11}[CO^*_{2(aq)}][MOH_{(aq)}]$, where $[i]$ is the concentration of species i in the aqueous solution.

Table 2
Kinetic constants in infinitely diluted solutions, computed with the correlations of Wylock et al. (2011) and Gondal et al. (2015) for a temperature of 20 °C.

Kinetic constant	Units	Value
k_{11}	$L\,mol^{-1}\,s^{-1}$	6.6×10^3
k_{12}	s^{-1}	1.0×10^{-4}
k_{21}	$L\,mol^{-1}\,s^{-1}$	1.0×10^{10}
k_{22}	s^{-1}	1.6×10^6

Table 3
Diffusion coefficients D_i, solutal expansion coefficients α_i, diffusivity ratios δ_i and solutal Rayleigh number R_i of the involved chemical species (Sihnel and Novotny, 1985; García, 2001; Almarcha et al., 2011; Haynes, 2012). The coefficients marked with "*" were measured experimentally in this study because not available in the literature. Data for reactants MOH are in green, data for products M_2CO_3 are in red.

Species i	D_i $[10^{-9}$ m^2/s$]$	α_i $[10^{-2}$ L/mol$]$	δ_i	R_i $[10^{-4}]$	$R_C/2 - R_B$ $[10^{-4}]$	δ_C/δ_B
CO_2	1.67	0.82	1.00	0.31		
LiOH	1.72	2.7	1.03	1.03	0.40	0.58
Li_2CO_3	0.99	7.6*	0.59	2.86		
NaOH	2.13	4.4	1.28	1.65	0.32	0.54
Na_2CO_3	1.16	10.5	0.70	3.94		
KOH	2.86	4.8	1.71	1.79	0.44	0.50
K_2CO_3	1.42	11.8	0.85	4.46		
CsOH	2.96	13.0	1.77	4.89	0.44	0.49
Cs_2CO_3	1.46	28.3*	0.87	10.67		

5.1.2. Reaction–diffusion equations for the concentration profiles

Assuming that the host solution is dilute enough to neglect non-ideal effects and that ions are transported in pairs due to local electroneutrality, the 1D concentration profiles are computed in the aqueous solution as solutions of the following dimensionless RD equations:

$$\frac{\partial A}{\partial t} = \frac{\partial^2 A}{\partial z^2} - AB, \tag{9a}$$

$$\frac{\partial B}{\partial t} = \delta_B \frac{\partial^2 B}{\partial z^2} - 2AB, \tag{9b}$$

$$\frac{\partial C}{\partial t} = \delta_C \frac{\partial^2 C}{\partial z^2} + AB, \tag{9c}$$

where A, B, and C are the concentrations of $CO^*_{2(aq)}$, $MOH_{(aq)}$, and $M_2CO_{3(aq)}$, respectively. $\delta_i = D_i/D_{CO_2}$ is the ratio between the diffusivity D_i of species i and D_{CO_2} the molecular diffusion coefficient of CO_2 in water (see Table 3). Note that the dimensionless rate of reaction (8) is equal to AB, the dimensionless speed of the limiting step (6). These equations are similar to those previously studied in the case of convective dissolution in reactive solutions (Budroni et al., 2014; Loodts et al., 2014a, 2015). They differ however from these previous works by the facts that (i) B disappears twice as fast as A because of reaction scheme (8) and (ii) differential diffusion ($\delta_i \neq 1$) is here explicitly taken into account. As will be shown below, the latter is important to understand the experimental trends.

The upper boundary located at the vertical coordinate $z = 0$ is the gas–liquid interface saturated with CO_2 and impenetrable to the other solutes, while the lower boundary at $z \to \infty$ represents the bulk of the host solution where only B is present, as we only consider the early-stage development of the instability. Eqs. (9) are solved using the boundary conditions

$$A(z=0) = 1; \quad A(z \to \infty) = 0, \tag{10a}$$

$$\frac{\partial B}{\partial z}(z=0) = 0; \quad B(z \to \infty) = \beta, \tag{10b}$$

$$\frac{\partial C}{\partial z}(z=0) = 0; \quad C(z \to \infty) = 0, \tag{10c}$$

and the initial conditions

$$A(z=0) = 1; \quad A(z>0) = 0, \tag{11a}$$

$$B = \beta, \tag{11b}$$

$$C = 0. \tag{11c}$$

Here, $\beta = B_0/A_0$ is the ratio between B_0 the initial concentration of the dissolved reactant MOH, and A_0 the solubility of CO_2 into water computed from Henry's law (Li and Lee, 1996) (see equilibrium (1)). We indeed assume that the concentrations in the host solution are not large enough to significantly modify the solubility of CO_2 in water. Table 1 gives β as a function of B_0 for the conditions of the experiments of this study.

Eqs. (9)–(11) do not admit general analytical solutions, so that the 1D concentration profiles solutions of Eqs. (9) are computed numerically using an Euler scheme (Faires and Burden, 2012). The total length of the system is 500 and is taken large enough so that the lower boundary does not affect the profiles. The mesh size is 1.0 and the time step is 0.02.

5.1.3. Equation of state for the density of the solution

The dimensionless density profile $\rho(z,t)$ in the aqueous phase is computed from the RD concentration profiles solutions of Eqs. (9) as

$$\rho = R_A A + R_B B + R_C C, \tag{12}$$

where $R_i = \frac{\alpha_i A_0 g l_c^3}{\nu D_{CO_2}}$ is the solutal Rayleigh number representing the contribution of species i to the density of the aqueous solution (see Table 3), with $g = 9.81$ m s^{-2} the norm of the gravity field, $\nu = 1.00 \times 10^{-6}$ m^2 s^{-1} the dynamic viscosity of water (Haynes, 2012), $D_{CO_2} = 1.67 \times 10^{-9}$ m^2 s^{-1} the diffusion coefficient of CO_2 in water (Haynes, 2012), and $l_c = \sqrt{\frac{D_{CO_2}}{k_{11}A_0}} = 2.56 \times 10^{-6}$ m the characteristic reaction-diffusion length (Rongy et al., 2008, 2010). $\alpha_i = \frac{1}{\rho_0}\frac{\partial \rho_d}{\partial [i]}$ is the solutal expansion coefficient of species i (see Table 3), where ρ_d and ρ_0 are the dimensional density of the solution and of the pure solvent (i.e. water), respectively. Note that here the characteristic time scale $t_c = 1/(k_{11}A_0)$ of the reaction is equal to 3.93×10^{-3} s.

5.1.4. Parameters

Table 3 shows the diffusion and solutal expansion coefficients used to compute the diffusivity ratios δ_i and the solutal Rayleigh number R_i. The diffusion coefficient increases when going down the column of alkali metals:

$$D_{LiOH} < D_{NaOH} < D_{KOH} < D_{CsOH} \tag{13}$$

and

$$D_{Li_2CO_3} < D_{Na_2CO_3} < D_{K_2CO_3} < D_{Cs_2CO_3}. \tag{14}$$

This increase can be related to the increase of the atomic radius. With the same positive charge of the alkali metal cation, the largest the radius of the ion, the smallest the solvation shell. For instance, the CsOH ion pair diffuses the fastest because its interactions with

water molecules are weaker than for the other alkali metal elements. In parallel, the solutal expansion coefficient α_i increases when going down the group of alkali metals, due to the increasing weight of the alkali metal ion. We have indeed

$$\alpha_{LiOH} < \alpha_{NaOH} < \alpha_{KOH} < \alpha_{CsOH}, \quad (15)$$

and

$$\alpha_{Li_2CO_3} < \alpha_{Na_2CO_3} < \alpha_{K_2CO_3} < \alpha_{Cs_2CO_3}. \quad (16)$$

The product Cs_2CO_3 is characterized by the largest solutal expansion and diffusion coefficients of all species considered here.

5.2. Density profiles in reactive solutions

A typical density profile building up in time in the host solution during an experiment with CsOH is shown in Fig. 11. In the bulk of the solution (large z), the reactant B = CsOH has not been consumed yet and is the only species present in dimensionless concentration β. The related density (12) is therefore equal to $R_B\beta$. By contrast, near the interface ($z = 0$), CsOH has been consumed by the reaction. There, the main contributions to the density are thus those of dissolved A = CO_2 and C = Cs_2CO_3, as CO_2 dissolves into the host solution from the interface and Cs_2CO_3 is produced at a reaction front which moves away in time from the interface due to the interplay between reaction and diffusion (Galfi and Rácz, 1988). The density at the interface is equal to $R_A + R_C C|_{z=0}$, with $C|_{z=0} > \beta/2$ here because of differential diffusivity. Given that the solutal expansion coefficient of Cs_2CO_3 is approximately 30 times larger than that of CO_2 (see Table 3), Cs_2CO_3 contributes much more to the density than CO_2. The contribution of the product to density adds to that of CO_2 and makes the upper fluid layer denser than in the non-reactive case, which has a destabilizing effect.

Let us now discuss the global shape of the density profile in the host solution (Fig. 11). The density profile has a minimum, where locally less dense fluid lies on top of a denser one, unlike its counterpart in the case of equal diffusion coefficients and A + B → C stoichiometry, which is monotonically decreasing (Loodts et al., 2014a). The difference in the diffusion coefficients of the salt product and the base reactant explains the minimum of density appearing here. The diffusion coefficient of MOH is indeed larger than that of M_2CO_3 for all tested M^+ (see Table 3). In other words, MOH diffuses faster than M_2CO_3, which creates a depleted zone below the reaction front as the product lags behind the reaction front at the top of the solution. Despite the presence of a minimum, the density stratification is more buoyantly unstable than its non-reactive counterpart as the density jump in the upper fluid layer is larger due to the higher concentration of the product M_2CO_3. We conclude that the minimum of density does not act here as a stabilizing barrier like in other systems (Loodts et al., 2014a; Budroni et al., 2014) where it originates from solutal effects only. Furthermore, the density difference between the minimum and the bulk is here small compared to the density of the upper fluid layer and hence, we suppose that during the development of the instability, fingers of denser fluid will outgrow the minimum.

5.3. Comparison of density profiles for different concentrations and reactants

To understand why convection is enhanced in experiments when increasing concentrations, or taking a counter-ion M^+ further down the alkali metal column, let us compare the density profiles when the initial concentration β of MOH or type of counter-ion M^+ are varied (see Tables 1 and 3). Because the density of the host solution differs largely among all non-reactive and reactive cases, we compare them by computing normalized density profiles $\Delta\rho(z) = \rho(z) - \rho(z=0)$ with $\rho(z=0)$ the density at the gas–liquid interface (Figs. 12 and 13).

Before further analyzing the effect of changing the concentration of the base, we describe the non-reactive (NR) profile corresponding to the case $\beta = 0$. Dissolved CO_2 diffuses in the aqueous solution from the gas–liquid interface. The NR density profile follows the analytical expression $\rho(z) = R_A\left[1 - \mathrm{erf}\left(\frac{z}{2\sqrt{t}}\right)\right]$ (Slim et al., 2013; Loodts et al., 2014b), and $\Delta\rho(z)$ is equal to

$$\Delta\rho(z) = -R_A\left[\mathrm{erf}\left(\frac{z}{2\sqrt{t}}\right)\right]. \quad (17)$$

Upon dissolution, CO_2 increases the density of the aqueous solution (see Table 3), and R_A is thus positive. In that case, $\Delta\rho(z)$ is negative, as denser fluid rich in dissolved CO_2 lies on top of less dense fluid. A buoyantly unstable density stratification builds up over time, which results in the classical dissolution-driven convective instability (Huppert and Neufeld, 2014; Loodts et al., 2014b; Emami-Meybodi et al., 2015).

To understand the influence on convection of changing the concentration of reactant for a given MOH (Figs. 7–9), the density

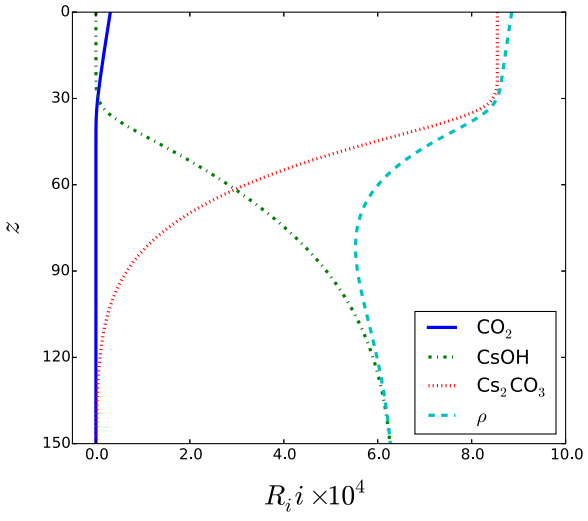

Fig. 11. RD contributions to density $R_i i(z)$ and density $\rho(z)$ profiles for time 1000, $M^+ = Cs^+$, and $\beta = 1.31$ corresponding to $[CsOH_{(aq)}] = 0.05$ M.

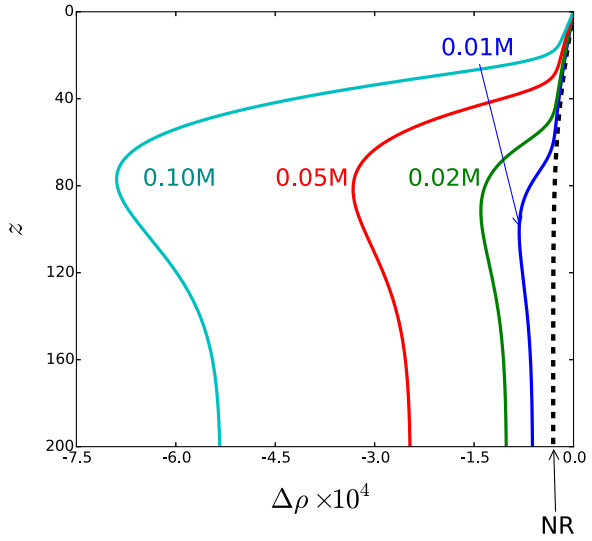

Fig. 12. RD normalized density profiles $\Delta\rho(z) = \rho(z) - \rho(z=0)$ for time 1000 and $M^+ = Cs^+$ in various concentrations. The non-reactive (NR) case is the black dashed curve.

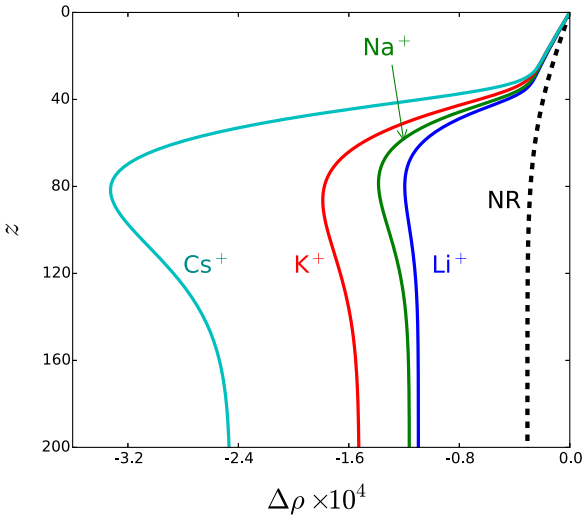

Fig. 13. RD normalized density profiles $\Delta\rho(z) = \rho(z) - \rho(z=0)$ for time 1000 and $\beta = 1.3$ corresponding to $[MOH_{(aq)}] = 0.05$ M. The non-reactive (NR) case is the black dashed curve.

profiles are compared for different initial concentration ratios β in Fig. 12. At a given time the amplitude of the upper density jump increases with β, i.e. when the concentration of reactant MOH is increased. The corresponding density profile is thus more buoyantly unstable, in agreement with the experimental results.

To explain the influence on convection of changing the counterion M^+ for a fixed concentration of reactant (Figs. 7, 8 and 10), the density profiles corresponding to different reactants MOH for the same initial concentration are compared at a given time in Fig. 13. The amplitude of the upper density jump increases in the sequence $Li^+ < Na^+ < K^+ < Cs^+$. This is coherent with the faster development of convection observed in the same sequence experimentally.

Note that these conclusions are not dependent on the time at which the density profiles are computed. Indeed, although the magnitude of the difference $|\Delta\rho_m|$ between the minimum of density and the density at the interface increases in time, it always increases at a given time in the same sequence $Li^+ < Na^+ < K^+ < Cs^+$ (see Fig. 14), and similarly for increasing concentrations (not shown here). The time at which the density profiles are compared can thus be chosen arbitrarily. For future quantitative modeling, a linear stability analysis or non-linear simulations should be performed to determine the onset time of the instability before which the RD density profile remains the correct reference.

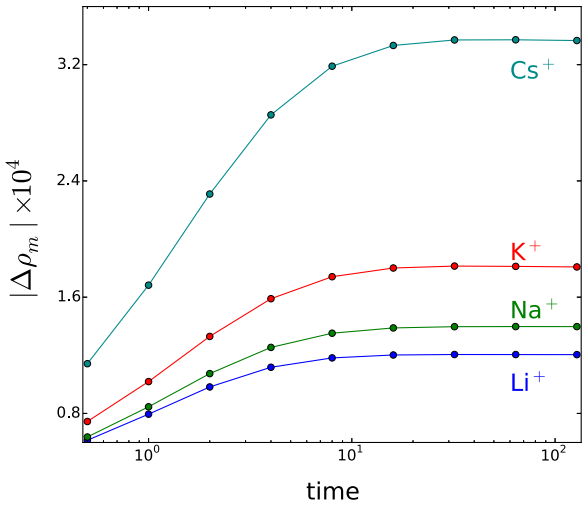

Fig. 14. $|\Delta\rho_m|$ defined as the difference between the minimum of density and the density at the interface, as a function of time, for all tested alkali cations at $[MOH_{(aq)}] = 0.05$ M.

6. Solutal versus differential diffusion effects

We now look at solutal and diffusivity effects separately to analyze the relative importance of density and diffusion-related effects on the dynamics. To do so, we compute the density profiles isolating each effect with a view to understanding whether the difference in the convective trend between the cations come from a difference in their solutal expansion coefficients, from a difference in their diffusion coefficients or from a combination of both solutal and diffusive effects.

6.1. Isolating solutal effects

To isolate the effect of the solutal expansion coefficients on the density profile in solution, the diffusion coefficients of all species are imposed equal (Loodts et al., 2014a, 2015). In that case, Eq. (9b) and $2 \times$ Eq. (9c) can be added to show that $B + 2C$ is a conserved quantity equal to β. By inserting $C = (\beta - B)/2$ into Eq. (12), the density profile for $\delta_i = 1$ is then written as

$$\rho = R_A A - \left(\frac{R_C}{2} - R_B\right) B + \frac{R_C \beta}{2}. \tag{18}$$

Eq. (18) shows that, for equal diffusion coefficients, R_A and $R_C/2 - R_B$ are the solutal parameters affecting the relative weight of A and B in the density stratification of the host solution, and thus controlling the growth rate of the instability. As seen in Table 3, $R_C/2 - R_B$ does not increase in the experimental sequence $Li^+ < Na^+ < K^+ < Cs^+$, which means that the solutal effect alone is not sufficient to explain the experimental results. Fig. 15 confirms indeed that for equal diffusion coefficients, the amplitude $|\Delta\rho_m|$ does not increase in the experimental sequence but rather increases as $R_C/2 - R_B$ does.

6.2. Isolating diffusive effects

To isolate the differential diffusivity effect, we arbitrarily impose the same Rayleigh numbers for all M^+ (for example $R_B = R_A$ and $R_C = 2R_A$) and examine the effect of varying δ_C/δ_B. When going down the alkaline column of the periodic table, δ_C/δ_B decreases, i.e. the salt diffuses increasingly slower compared to the base from Li^+ to Cs^+ (see Table 3). As explained above, this slower diffusion of the salt results in the fact that the product lags behind the reaction

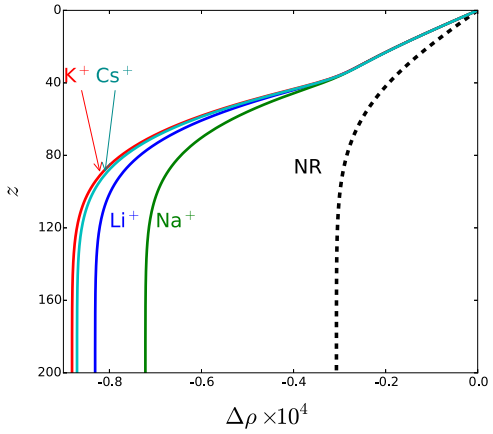

Fig. 15. Same as in Fig. 13, in the case of equal δ_i ($\delta_B = \delta_C = 1$ for all counter-ions M^+). The absence of differential diffusion suppresses the minimum and a stability sequence different from the one observed in experiments is predicted.

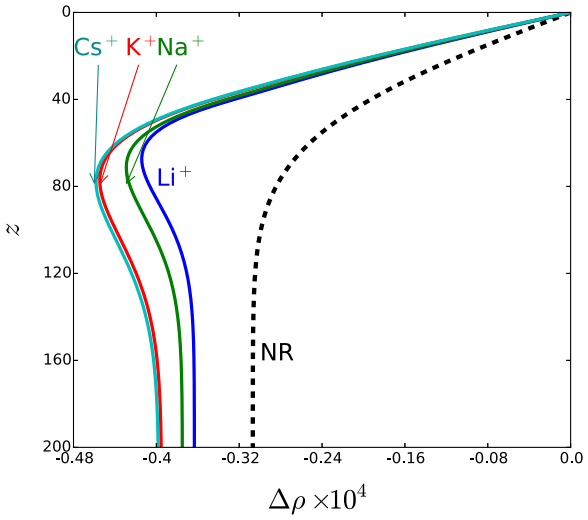

Fig. 16. Same as in Fig. 13, in the case of equal R_i ($R_B = R_A$ and $R_C = 2R_A$ for all counter-ions M^+) but with differential diffusion coefficients ($\delta_i \neq 1$). The stability sequence is the same as the one observed in experiments.

front at the top of the solution, which makes the density stratification more buoyantly unstable. The decrease of δ_C/δ_B when going down the alkaline column of the periodic table can thus explain the relative stability of the systems tested here. Fig. 16 shows that the difference between the density at the interface and the minimum of density indeed increases in the sequence $Li^+ < Na^+ < K^+ < Cs^+$ as δ_C/δ_B decreases. The amplitude of the changes are nevertheless smaller than those when both differential diffusion ($\delta_i \neq 1$) and solutal effects are combined (see Fig. 13). Note that these conclusions hold for arbitrary values of the Rayleigh numbers as long as they are the same for all the studied alkali. The much more unstable behavior of CsOH observed experimentally (Fig. 7), in particular compared to the non-reactive case, results thus from a combination of both diffusive and solutal effects.

7. Discussion

In summary, the influence of chemical reactions on the convective instability can be understood by analyzing the shape of the density profile. Chemical reactions alter this density profile by changing the concentrations of the solutes and thus modify the development of the instability. By evaluating solutal and differential diffusivity contributions to the density profile, the trends observed experimentally can be interpreted, i.e. convection is enhanced (i) in the reactive systems compared to their non-reactive counterpart, (ii) when the concentration of the initially dissolved reactant is increased, and (iii) when changing the counter-ion M^+ in the sequence $Li^+ < Na^+ < K^+ < Cs^+$. Our theoretical analysis gives thus a good support to interpret the experiments.

Note that all these conclusions should be recovered both in porous media flows (governed by Darcy's law) and other flows (described by Stokes or Navier–Stokes equations) as they are independent of the flow equation used. Further techniques such as linear stability analyses or non-linear simulations are needed to quantitatively assess the stability of these profiles with regard to convection. However, as an unstable density stratification is at the origin of the convective instability, the qualitative comparison of the unstable density gradient and the extent of the denser zone for different initial concentrations or types of reactants has already allowed to interpret the trends observed in the experiments.

8. Conclusions

We have experimentally compared the density-driven convection developing upon dissolution of gaseous CO_2 into water and alkaline aqueous solutions of LiOH, NaOH, KOH and CsOH in increasing concentrations. In these reactive solutions, the dissolution and mixing of CO_2 is enhanced thanks to chemical reactions occurring between the base and dissolved CO_2, which produce a salt with a larger solutal expansion coefficient and smaller diffusion coefficient than both reactants. In these conditions, the convective instability arises sooner and develops faster (i) when the concentration of the base in the aqueous solution is increased; (ii) when the spectator ion M^+ is changed going down the alkali metal column, i.e. fingering is the slowest for LiOH and the intensity of convective mixing increases following the series LiOH < NaOH < KOH < CsOH. These observations were explained by computing numerically the RD density profiles setting up in the aqueous solution upon CO_2 dissolution. These profiles show that both differences in diffusion and solutal expansion coefficients of all chemical species must be taken into account to explain the active role of the counter-ion M^+ observed experimentally. Furthermore, the density profiles explain that, for any reactant MOH, increasing the concentration enhances the convective dissolution because it increases the amplitude of the unfavorable density jump at the source of the instability.

Our results show that the nature and the concentration of reactants are important parameters to understand the development of the density-driven instability in reactive solutions. In fact, the spectator ion M^+, which does not actively participate in the acid–base reaction, plays nevertheless a major role in the development of the instability by acting explicitly on the density profile at the very source of the convective instability.

In the context of CO_2 sequestration, this suggests that chemical reactions should not be neglected if realistic quantitative predictions of CO_2 fluxes or the shutdown time of the aquifer are to be computed. Moreover, the characteristics of so-called "spectator ions" appear to be of tantamount importance as their very nature impacts the density of the solution. An analysis of the chemical composition of a candidate sequestration site should therefore be a prerequisite to assess its potential efficiency in dissolving CO_2. Understanding how the chemistry of the site can stabilize or destabilize convective dissolution is of peculiar interest for more accurate predictions of the time needed to saturate a site with CO_2 or evaluate its storage capacity.

Acknowledgments

We thank S. Dehaeck, H. Baudine, F. Brau, G. Schuszter, I. Berenstein, and L. Lemaigre for fruitful discussions. V. Loodts is F.R.S.-FNRS Research Fellow. Funding by Prodex, ARC CONVINCE, and PDR-FNRS FORECAST projects is gratefully acknowledged.

Appendix A. Supplementary data

Supplementary data associated with this article can be found, in the online version, at http://dx.doi.org/10.1016/j.ijggc.2016.07.034.

References

Almarcha, C., Trevelyan, P.M.J., Riolfo, L.A., Zalts, A., El Hasi, C., D'Onofrio, A., De Wit, A., 2010. Active role of a color indicator in buoyancy-driven instabilities of chemical fronts. J. Phys. Chem. Lett. 1, 752–757.

Almarcha, C., R'Honi, Y., De Decker, Y., Trevelyan, P.M.J., Eckert, K., De Wit, A., 2011. Convective mixing induced by acid–base reactions. J. Phys. Chem. B 115, 9739–9744.

Andres, J.T.H., Cardoso, S.S.S., 2011. Onset of convection in a porous medium in the presence of chemical reaction. Phys. Rev. E 83, 046312.

Andres, J.T.H., Cardoso, S.S.S., 2012. Convection and reaction in a diffusive boundary layer in a porous medium: nonlinear dynamics. Chaos 22, 037113.
Backhaus, S., Turitsyn, K., Ecke, R.E., 2011. Convective instability and mass transport of diffusion layers in a Hele-Shaw geometry. Phys. Rev. Lett. 106, 104501.
Budroni, M.A., Riolfo, L.A., Lemaigre, L., Rossi, F., Rustici, M., De Wit, A., 2014. Chemical control of hydrodynamic instabilities in partially miscible two-layer systems. J. Phys. Chem. Lett. 5, 875–881.
Cardoso, S.S.S., Andres, J.T.H., 2014. Geochemistry of silicate-rich rocks can curtail spreading of carbon dioxide in subsurface aquifers. Nat. Commun. 5, 6743.
Emami-Meybodi, H., Hassanzadeh, H., Green, C.P., Ennis-King, J., 2015. Convective dissolution of CO_2 in saline aquifers: progress in modeling and experiments. Int. J. Greenh. Gas Control 40, 238–266.
Ennis-King, J., Paterson, L., 2005. Role of convective mixing in the long-term storage of carbon dioxide in deep saline formations. SPE J. 10, 1–12.
Ennis-King, J., Paterson, L., 2007. Coupling of geochemical reactions and convective mixing in the long-term geological storage of carbon dioxide. Int. J. Greenh. Gas Control 1, 86–93.
Faires, J.D., Burden, R., 2012. Numerical Methods, 4th edition. Brooks/Cole, Cengage Learning.
Faisal, T.F., Chevalier, S., Sassi, M., 2013. Experimental and numerical studies of density driven natural convection in saturated porous media with application to CO_2 geological storage. Energy Procedia 37, 5323–5330.
Faisal, T.F., Chevalier, S., Bernabe, Y., Juanes, R., Sassi, M., 2015. Quantitative and qualitative study of density driven CO_2 mass transfer in a vertical Hele-Shaw cell. Int. J. Heat Mass Transf. 81, 901–914.
Galfi, L., Rácz, Z., 1988. Properties of the reaction front in an $A + B \rightarrow C$ type reaction–diffusion process. Phys. Rev. A 38, 3151.
García, J.E., 2001. Density of Aqueous Solutions of CO_2. Lawrence Berkeley National Laboratory.
Ghesmat, K., Hassanzadeh, H., Abedi, J., 2011. The impact of geochemistry on convective mixing in a gravitationally unstable diffusive boundary layer in porous media: CO_2 storage in saline aquifers. J. Fluid Mech. 673, 480–512.
Gondal, S., Asif, N., Svendsen, H.F., Knuutila, H., 2015. Kinetics of the absorption of carbon dioxide into aqueous hydroxides of lithium, sodium and potassium and blends of hydroxides and carbonates. Chem. Eng. Sci. 123, 487–499.
Hassanzadeh, H., Pooladi-Darvish, M., Keith, D.W., 2005. Modeling of convective mixing in CO_2 storage. J. Can. Pet. Technol. 44, 43–51.
Haynes, W.M., 2012. CRC Handbook of Chemistry and Physics. CRC Press.
Hikita, H., Asai, S., Takatsuka, T., 1976. Absorption of carbon dioxide into aqueous sodium hydroxide and sodium carbonate-bicarbonate solutions. Chem. Eng. J. 11, 131–141.
Huppert, H.E., Neufeld, J.A., 2014. The fluid mechanics of carbon dioxide sequestration. Annu. Rev. Fluid Mech. 46, 255–272.
Kim, M.C., Choi, C.K., 2014. Effect of first-order chemical reaction on gravitational instability in a porous medium. Phys. Rev. E 90, 053016.
Kim, M.C., Kim, Y.H., 2015. The effect of chemical reaction on the onset of gravitational instabilities in a fluid saturated within a vertical Hele-Shaw cell: theoretical and numerical studies. Chem. Eng. Sci. 134, 632–647.
Kneafsey, T.J., Pruess, K., 2010. Laboratory flow experiments for visualizing carbon dioxide-induced, density-driven brine convection. Transp. Por. Med. 82, 123–139.
Kneafsey, T.J., Pruess, K., 2011. Laboratory experiments and numerical simulation studies of convectively enhanced carbon dioxide dissolution. Energy Procedia 4, 5114–5121.
Kuster, S., Riolfo, L.A., Zalts, A., El Hasi, C., Almarcha, C., Trevelyan, P.M.J., De Wit, A., D'Onofrio, A., 2011. Differential diffusion effects on buoyancy-driven instabilities of acid–base fronts: the case of a color indicator. Phys. Chem. Chem. Phys. 13, 17295–17303.
Li, M.-H., Lee, W.-C., 1996. Solubility and diffusivity of N_2O and CO_2 in (Diethanolamine + N-methyldiethanolamine + water) and in (diethanolamine + 2-amino-2-methyl-1-propanol + water). J. Chem. Eng. Data 41, 551–556.
Loerting, T., Tautermann, C., Kroemer, R.T., Kohl, I., Hallbrucker, A., Mayer, E., Liedl, K.R., 2000. On the surprising kinetic stability of carbonic acid (H_2CO_3). Angew. Chem. Int. Ed. 39, 891–894.
Loodts, V., Thomas, C., Rongy, L., De Wit, A., 2014a. Control of convective dissolution by chemical reactions: general classification and application to CO_2 dissolution in reactive aqueous solutions. Phys. Rev. Lett. 113, 114501.
Loodts, V., Rongy, L., De Wit, A., 2014b. Impact of pressure, salt concentration, and temperature on the convective dissolution of carbon dioxide in aqueous solutions. Chaos 24, 043120.
Loodts, V., Rongy, L., De Wit, A., 2015. Chemical control of dissolution-driven convection in partially miscible systems: theoretical classification. Phys. Chem. Chem. Phys. 17, 29814–29823.
Mojtaba, S., Behzad, R., Rasoul, N.M., Mohammad, R., 2014. Experimental study of density-driven convection effects on CO_2 dissolution rate in formation water for geological storage. J. Nat. Gas Sci. Eng. 21, 600–607.
Neufeld, J.A., Hesse, M.A., Riaz, A., Hallworth, M.A., Tchelepi, H.A., Huppert, H.E., 2010. Convective dissolution of carbon dioxide in saline aquifers. Geophys. Res. Lett. 37, L22404.
Outeda, R., El Hasi, C., D'Onofrio, A., Zalts, A., 2014. Experimental study of linear and nonlinear regimes of density-driven instabilities induced by CO_2 dissolution in water. Chaos 24, 013135.
Pohorecki, R., Moniuk, W., 1988. Kinetics of reaction between carbon dioxide and hydroxyl ions in aqueous electrolyte solutions. Chem. Eng. Sci. 43, 1677–1684.
Rochelle, C.A., Czernichowski-Lauriol, I., Milodowski, A.E., 2004. The impact of chemical reactions on CO_2 storage in geological formations: a brief review. Geol. Soc. Lond. Spec. Publ. 233, 87–106.
Rongy, L., Trevelyan, P.M.J., De Wit, A., 2008. Dynamics of $A + B \rightarrow C$ reaction fronts in the presence of buoyancy-driven convection. Phys. Rev. Lett. 101, 084503.
Rongy, L., Trevelyan, P.M.J., De Wit, A., 2010. Influence of buoyancy-driven convection on the dynamics of $A + B \rightarrow C$ reaction fronts in horizontal solution layers. Chem. Eng. Sci. 65, 2382–2391.
Settles, G.S., 2001. Schlieren and Shadowgraph Techniques: Visualizing Phenomena in Transparent Media. Springer-Verlag.
Sihnel, O., Novotny, P., 1985. Densities of Aqueous Solutions of Inorganic Substances. Elsevier.
Slim, A.C., Bandi, M.M., Miller, J.C., Mahadevan, L., 2013. Dissolution-driven convection in a Hele-Shaw cell. Phys. Fluids 25, 024101.
Thomas, C., Lemaigre, L., Zalts, A., D'Onofrio, A., De Wit, A., 2015. Experimental study of CO_2 convective dissolution: the effect of color indicators. Int. J. Greenh. Gas Control 42, 525–533.
Tian, H., Xu, T., Wang, F., Patil, V.V., Sun, Y., Yue, G., 2014. A numerical study of mineral alteration and self-sealing efficiency of a caprock for CO_2 geological storage. Acta Geotech. 9, 87–100.
Vas Bhat, R.D., Kuipers, J.A.M., Versteeg, G.F., 2000. Mass transfer with complex chemical reactions in gas–liquid systems: two-step reversible reactions with unit stoichiometric and kinetic orders. Chem. Eng. J. 76, 127–152.
Ward, T.J., Cliffe, K.A., Jensen, O.E., Power, H., 2014a. Dissolution-driven porous-medium convection in the presence of chemical reaction. J. Fluid Mech. 747, 316–349.
Ward, T.J., Jensen, O.E., Power, H., Riley, D.S., 2014b. High-Rayleigh-number convection of a reactive solute in a porous medium. J. Fluid Mech. 760, 95–126.
Wylock, C., Dehaeck, S., Cartage, T., Colinet, P., Haut, B., 2011. Experimental study of gas–liquid mass transfer coupled with chemical reactions by digital holographic interferometry. Chem. Eng. Sci. 66, 3400–3412.
Wylock, C., Rednikov, A., Haut, B., Colinet, P., 2014. Nonmonotonic Rayleigh-Taylor instabilities driven by gas–liquid CO_2 chemisorption. J. Phys. Chem. B 118, 11323–11329.
Xu, T., Spycher, N., Sonnenthal, E., Zheng, L., Pruess, K., 2012. TOUGHREACT User's Guide: a simulation program for non-isothermal multiphase reactive transport in variably saturated geologic media, version 2.0. Report LBNL-DRAFT. Lawrence Berkeley National Laboratory, Berkeley.
Zeebe, R.E., Wolf-Gladrow, D., 2001. CO_2 in Seawater: Equilibrium, Kinetics, Isotopes. Elsevier.
Zhang, W., Li, Y., Omambia, A.N., 2011. Reactive transport modeling of effects of convective mixing on long-term CO_2 geological storage in deep saline formations. Int. J. Greenh. Gas Control 5, 241–256.